Ceramics International 48 (2022) 7136–7144

Contents lists available at ScienceDirect

Ceramics International

journal homepage: www.elsevier.com/locate/ceramint

Ablation evolution of a new light weight silicon based thermal protection material in high temperature gas flow

Shilong Zhu [a], Jinsong Zhang [b,c], Mengkun Yue [b,c], Yunlong Tang [a,b,c,*], Wen Yue [a,g], Zhe Qu [b,c], Xian Wang [d], Lianzhong Chen [f], Yewei Gui [e], Xue Feng [b,c,**]

[a] School of Engineering and Technology, China University of Geosciences, Beijing, 100083, China
[b] AML, Department of Engineering Mechanics, Tsinghua University, Beijing, 100084, China
[c] Center for Mechanics and Materials, Tsinghua University, Beijing, 100084, China
[d] Flexible Integrated Circuit Center, Institute of Flexible Electronic Technology of THU, Jiaxing, 314006, China
[e] Sate Key Laboratory of Aerodynamics, China Aerodynamics Research and Development Center, Mianyang, 621000, China
[f] China Academy of Aerospace Aerodynamics, Beijing, 100074, China
[g] Zhengzhou Research Institute, China University of Geosciences (Beijing), Zhengzhou, 450001, China

ARTICLE INFO

Keywords:
Flat plate ablation
Droplets flow
High temperature wind tunnel
Two-color method
H–S optical flow method
Lagrangian particle tracking (LPT) method

ABSTRACT

High silicon oxygen/phenolic aldehyde (VSF/PR) ablative heat-proof material is widely used as resin-based heat-proof system for long-term aircraft. Understanding the generation and flow process of the surface droplets during high temperature is key to improving the thermal stability, and prior to which, a direct visualization of the surface evolution is required. Here we use optical imaging technique to in-situ and real time record the surface evolution of a flat plate subjected to thermal ablation at 1700 °C in wind tunnel. Based on the experimental results processed using image processing method and by combining the fluid theory in high temperature wind tunnel, we explained the distribution of the surface temperature and surface liquid droplets, the velocity field, and the movement of the liquid droplets on the plate surface. Results show that the distribution of the liquid droplets was correlated to the temperature distribution. A verification experiment for the merging process of two liquid droplets shows that droplet with high viscosity would generate a great friction force and cause the droplet to move forward in a rolling manner. The chasing and merging process of the liquid droplets with high viscosity is rather an entrainment process than a spontaneous merging process normally induced by surface tension. These findings help to understand the flow behavior of the liquid droplets during thermal ablation.

1. Introduction

The surface evolution of structural components at high temperatures under service conditions is currently poorly understood. The service conditions, including high temperature and high gas flux, usually lead to severe surface modification, where chemical reaction generating new phases (gaseous, liquid) and physical process where mechanical erosion occurs. Among these challenging topics, understanding surface liquid generation and its flow is of great importance to improve the thermal ablation resistance and thermal stability of the structures. While capturing the gaseous phase change is yet impossible, it is however, possible to visualize the real time surface evolution during thermal ablation. Real time and *in situ* information of these thermal, chemical and physical processes could fundamentally contribute to the understanding of the mechanisms of the fluid behavior of the surface liquids. For instance, Fang [1,2] et al. used optical method to capture the real time surface evolution on the surface of C/SiC (carbon fiber reinforced silicon carbide composites) and SiC subjected to oxyacetylene torch flame. The mechanisms of the typical surface structures including surface liquid droplet generation, flow, merging process as well as the "bone-like" structures due to material melting and flow were studied. This real time visualization method can be applied to thermal tests with more critical thermal loading.

Currently the experimental methods for thermal ablation tests include mainly the wind tunnel assessment, arc ablation [3], plasma torch [4] ablation, and oxyacetylene [5–7] ablation, etc. Among all the

* Corresponding author. School of Engineering and Technology, China University of Geosciences, Beijing, 100083, China.
** Corresponding author. AML, Department of Engineering Mechanics, Tsinghua University, Beijing, 100084, China.
E-mail addresses: tangyunlong@cugb.edu.cn (Y. Tang), fengxue@tsinghua.edu.cn (X. Feng).

https://doi.org/10.1016/j.ceramint.2021.11.273
Received 27 September 2021; Received in revised form 14 November 2021; Accepted 25 November 2021
Available online 2 December 2021

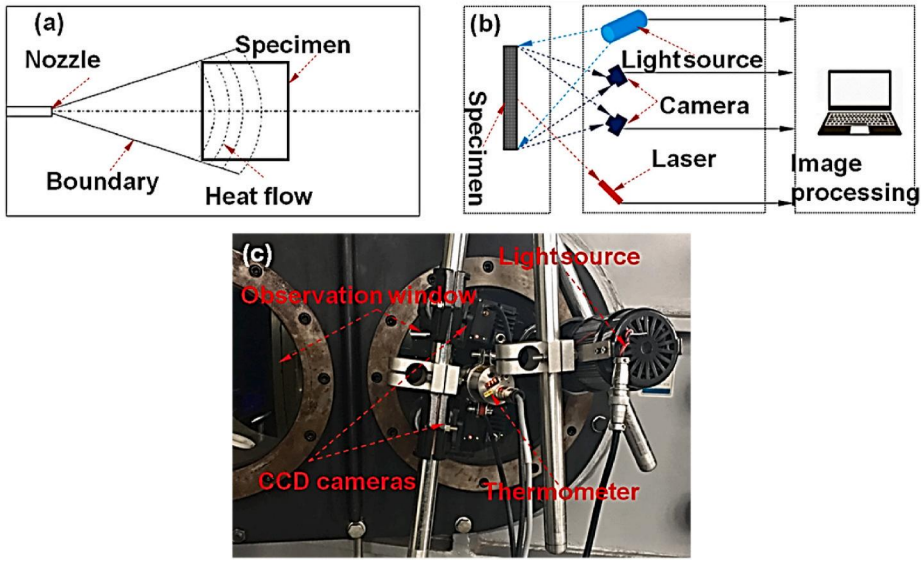

Fig. 1. (a–b) Schematic showing the experimental setup: gas flow interacting with plate specimen in wind tunnel in (a) and synchronous measurement of temperature and deformation in (b); (c) on-site experimental equipment.

testing methods, the wind tunnel assessment can maximum meet the environmental and experimental requirement that is close to the service conditions. However, testing in wind tunnel exerts great limitations to traditional measuring technique, making it challenging for real time capturing and measuring the ablation status of materials during the process of the test. Conventionally, the evaluation and analysis of the thermal ablation tests carried out under such experimental conditions are performed post-mortem, while the real time information on the evolution and degradation process of the material is missing. The off-line, discontinuous test and characterization method fail to ensure the accurate tracking of the experimental process in the high temperature environment [8].

Furthermore, it has been widely observed that during thermal ablation the sample surface goes through morphological changes including the generation of liquid droplets and liquid flow [2]. In order to characterize the liquid flow pattern and quantify the flow speed, it is possible to adopt the optical flow field method. The optical flow field refers to a two-dimensional (2D) instantaneous velocity field composed of all pixel points in an image. The 2D velocity vector is the projection of the 3D velocity vector of the visible points onto the image surface. Therefore, the optical flow not only contains the movement information of the targets (e.g., liquid droplets) being observed, but also contains the information of the 3D structure. In 1981, Horn and Shuck [9] proposed the H–S algorithm, and Lucas and Kanade proposed L-K algorithm [10]. Barron [11] et al. summarized various calculation methods of optical flow field. Later, various test and evaluation indexes of optical flow field were established and a comparison platform was provided for various methods, which greatly improved the calculation accuracy of optical flow field [12].

In addition to the optical flow field for potential measurement of the full field fluid flow, the Lagrangian velocity of the particles can be used for describing the local fluid velocity, and the trajectory of the particles is calculated by the dynamic equations. The model can be dated back to the Lagrange equation in 1987. Thomson [13] systematically summarized and improved the previous work, making it more widely used for the measurement of flow in fluids mechanics. It has been shown that particle tracking method is an effective method to reveal the law of fluid motion and has been widely used in many fields. Korotenko [14] et al. studied the size and fractal behavior of the trajectory of Lagrangian particles in a 2D turbulent flow field. Wang [15] et al. used Lagrangian particle tracking method to discuss the influence of the Bohai sea circulation in summer and winter, sea exchange and runoff into the sea on the Bohai sea circulation.

In this paper, we adopt the recently developed dual-lens (two camera) optical system to obtain simultaneously the temperature and deformation of the sample based on Su and Fang [16] et al.. Then we analyze the surface evolution during thermal ablation, including the liquid generation and flowing on the sample surface using optical flow method and Lagrangian particle tracking method. The understanding of the surface evolution processes may well serve as foundation for the surface microstructural design in order to modulate the phase transformation induced by thermo-chemical reactions. Alternatively, through better control of the liquid distribution via surface structure modification, it is expected to take full advantage of the liquid distributed on the surface to isolate the air from the substrate and to achieve, for instance, better thermal ablation resistance.

2. Preparation of materials and experimental setup

2.1. Preparation of materials

In plate ablation test, the sample material is high silicon oxide/phenolic composite material, which is made of high silicon oxide fiber, glass fiber, quartz fiber and decomposable fiber braided silicon-based fiber cloth reinforcement system, combined with phenolic resin filling [17,18]. Among them, the high melting point of quartz fibers can resist the erosion of heat flow for a period of time. The melting point of fiberglass is relatively low, in order to be a melt binder under long geothermal flow conditions; decomposable fibers are used to improve the decomposition efficiency of other fillers.

2.2. Experimental setup

Thermal ablation test on a flat plate was carried out in an arc-heated wind tunnel. The arc-heated wind tunnel provides a high temperature environment with quasi-uniform temperature distribution in the testing chamber. The temperature, testing time, and flow speed can be tailored for the target components/specimens. The high voltage arc generated by the arc-heater heats up the high-pressure gas flow that expands after passing through the nozzle and increases its speed to form high temperature jet flow. The sample clamped at the nozzle exit was then subjected to the high temperature jet flow for thermal ablation test, as illustrated in Fig. 1(a). The geometry of all the specimens (fabricated using high silica phenolic resin woven material) used in this work is

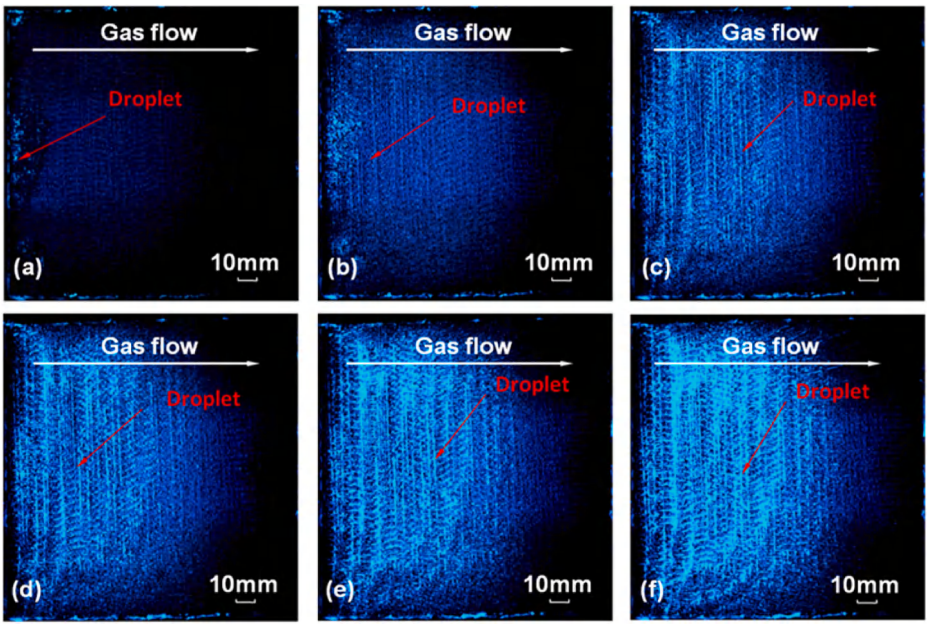

Fig. 2. Experimental results of plate ablation: (a) t = 3s; (b)t = 6s; (c) t = 9s; (d) t = 18s; (e) t = 24s; (f) t = 36s.

150mm × 150 mm in square shape. The contact angle between the flow direction and specimens in the experimental chamber is from 0° to 5°, the maximum velocity of gas flow is 2100 m/s, and the maximum temperature on the surface of the plate obtained by improved two-color method [16,19,20] is 1700 °C.

It is noted that the temperature on the plate subjected to thermal ablation process is below 3000 K, and the radiation energy is the strongest within the red light (R), followed by green light (G), and with blue light (B) being the weakest according to blackbody radiation theory. Thus, we adopted the reflective light from B channel for displacement measurement. R and G channels were used for temperature measurement with the improved two-color ratio method introduced in Ref. [16]. In addition, blue light source was used for light compensation [21]. The choice of using blue light for light compensation is to avoid the radiation effect for temperature measurement. The schematic of synchronous measurement of temperature and displacement is shown in Fig. 1(b) and (c).

2.3. Experimental results

In Fig. 2 it shows the results of thermal ablation of the flat pate in the wind tunnel. The surface of the flat plate at different times was acquired *in situ* and real time using a recently developed optical system [21–24]. The images in Fig. 2 appear to be blue is because of the band pass filter on the CCD camera we used to allow mainly the blue light through the camera lens when capturing the images. The advantage of using blue light is to suppress the thermal radiation [16], so that the surface evolution (e.g., surface liquid generation, liquid droplets flow) during

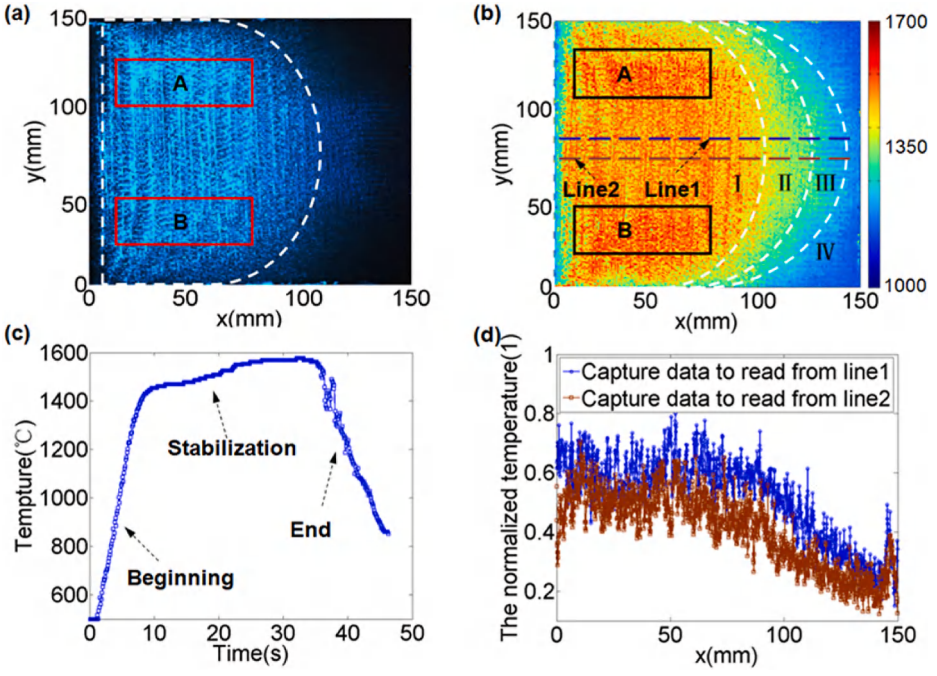

Fig. 3. Experimental results of plate ablation and surface temperature distribution: (a)surface morphology captured using real time optical system; (b)surface temperature field calculated using improved two-color method; (c)single-point temperature recorded using infrared pyrometer as a function of time; (d)normalized temperature on Line1 and Line2 along the gas flow. (For interpretation of the references to color in this figure legend, the reader is referred to the Web version of this article.)

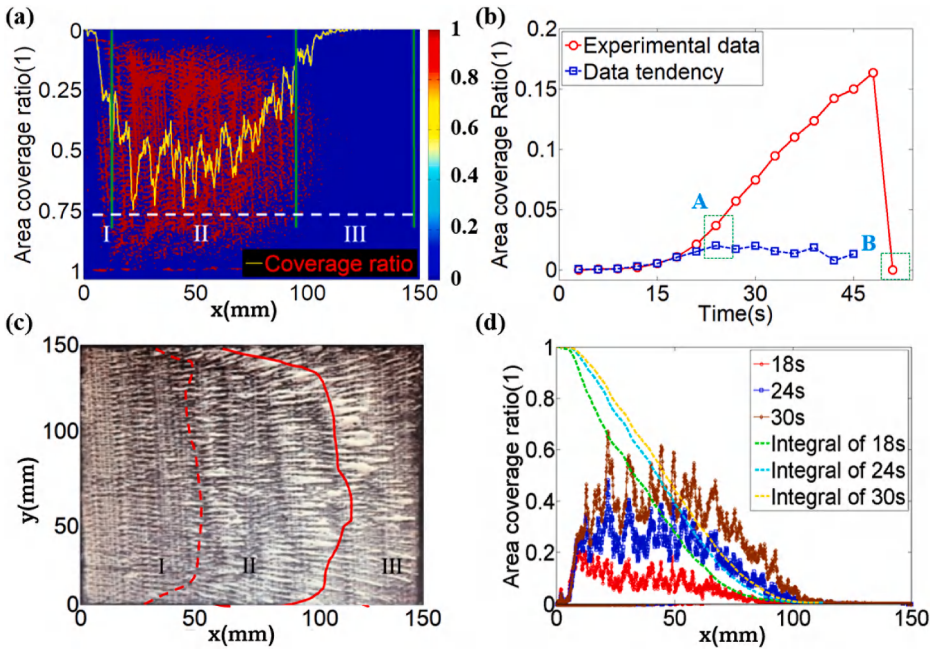

Fig. 4. Analysis of the liquid distribution generated on the surface during plate ablation: (a) droplet distribution extracted from the acquired images; (b) area coverage ratio of the liquid droplets on the plate surface as a function of time (red) and its rate of change (blue); (c) "frozen" droplet distribution on the plate surface after the experiment; (d) droplet coverage ratio along gas flow direction and its integral curves at different times. (For interpretation of the references to color in this figure legend, the reader is referred to the Web version of this article.)

thermal ablation can be real time obtained. The brighter regions on the surface correspond to the liquid droplets and the plate surface texture due to their higher reflectivity to the light.

The surface change in Fig. 2 indicates that complex physical and chemical changes have taken place on the plate surface (possibly also inside the plate) under the action of high temperature gas flow, and a large amount of liquid is generated on the surface. The surface is then analyzed in the following sections, with a focus on the surface temperature and liquid flow pattern to understand the thermal ablation mechanisms for the material.

3. Results and analyses

3.1. Surface temperature

In Fig. 3(a) a representative surface morphology of the plate due to thermal ablation is displayed. The surface of the plate was being ablated due to the high temperature flux, generating a large number of liquid droplets flowing on the surface. In Fig. 3(b), it shows the surface temperature field calculated using the improved two-color method. The spatial distribution of the temperature agrees very well with the free-jet flow profile. Based on the temperature field in Fig. 3(b), the plate surface subjected to thermal ablation can be divided into four regions (as indicated by the Roman numbers in Fig. 3(b)), namely, Region I where a large number of liquid droplets were generated due to the higher thermal flux; Region II the transition area from higher temperature to lower temperature; Region III the radiation dominated area; and Region IV which is least affected by the thermal flux. Note that in Region I the temperature is non-uniform, which is possibly caused by the local surface roughness and the non-uniformly distributed liquid droplets that evaporate by absorbing the heat. The temperature shows a peak in the symmetric regions A and B within Region I.

As a reference, Fig. 3(c) shows the single point surface temperature recorded using an infrared pyrometer (MI3, Raytek) as a function of the ablation time. Fig. 3(d) shows the temperature distribution at time t on the sample surface along Line1 and Line2 indicated by the dashed lines in Fig. 3(b). By comparing Fig. 3(c) and (d), the temperature distribution as a function of time from single-point pyrometer shows a similarity with that from the temperature integral from Line1 and Line2, suggesting a correlation between the spatial distribution of the temperature and the temporal change.

In high temperature wind tunnel, due to the fact that the viscosity is negligible compared to Reynolds stress, hence by ignoring the viscosity and other energy dispersion, then the thermal heat along the central of the free jet at time t can be simplified as [25]:

$$Q(t) = \alpha \frac{1}{l(t)^2} \tag{1}$$

where $Q(t)$ is heat at time t, $l(t)$ is distance to the source of free jet at time t, α is a constant. In addition, the thermal heat density $q(t)$ at time t can be expressed as:

$$q(t) = \frac{Q(t)}{S(t)t} = \alpha \frac{1}{S(t)tl(t)^2} \tag{2}$$

where $S(t)$ is the area of the cross-section. Thus, the thermal heat density on the plate surface is reciprocal to time. Furthermore, the thermal heat can be expressed in terms of temperature:

$$\int_{t_0}^{t} q(t) = \mu \frac{(T_1 - T_c)}{d} \tag{3}$$

where μ is thermal conductivity, T_1 is surface temperature, T_c is cold surface temperature that is assumed to be constant, d is plate thickness.

Combining **Eqs. (1)–(3)**, it gives:

$$(T_1 - T_c) = \frac{\alpha d}{\mu} \int_{t_0}^{t} \frac{1}{S(t)tl(t)^2} \tag{4}$$

Equation (4) shows that the spatial distribution of the temperature is correlated to the temporal change, namely, the single-point temperature changes temporally according to the spatial change of the flow. The tendency of the curves Line1 and Line2 in Fig. 3(d) satisfies with the free-jet flow theory as well. However, it is also noticed that the data in Line1 and Line2 shows larger fluctuation in comparison with that obtained from the pyrometer. This is attributed to the numerous liquid droplets floating on the sample surface that caused the non-uniform distribution of the temperature.

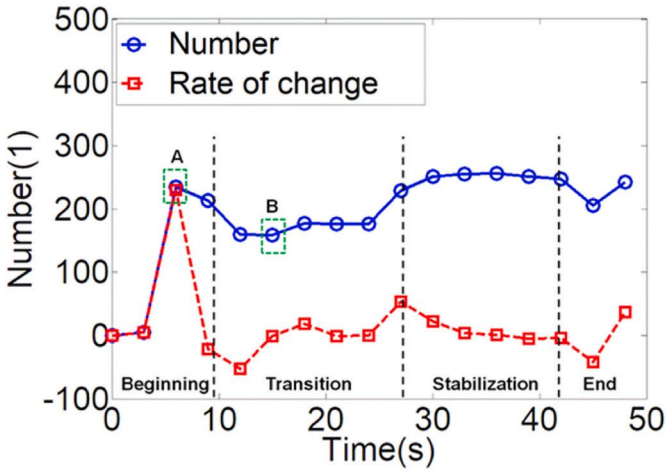

Fig. 5. Distribution of the number of discrete liquid droplets on the plate surface at different times: four stages were categorized and noted along with the curves.

3.2. Distribution of liquid droplets on the surface

The analysis of the distribution of the liquid on the plate surface is shown in Fig. 4. The distribution of the liquid droplets was processed by image extraction technique, namely, the Level Set method [26], which is a simple, accurate, and flexible numerical method that can separate the target from the image. One of the main advantages of this method is to process complex topological changes in the sequential images. When the image is segmented by the Level Set method, it is processed by morphological methods, as displayed in Fig. 4(a). The surface coverage of the liquid droplets as a function of time was calculated and displaced in Fig. 4(b). After the experiment, the sample was cooled down and the liquid droplets and their floating patterns were "frozen" and solidified on the surface, forming a morphology in Fig. 4(c). In Fig. 4(d) it shows the change of the surface coverage as well as its integral, of the liquid droplets along the gas flow direction at different ablation times.

By comparing Fig. 4(a) and (c), the distribution of the liquids on the surface can be divided into three regions, namely, Region I being the core ablation zone where the surface coverage of liquid is small due to the high-speed gas flux flushing away the freshly generated liquid droplets (mechanical erosion). Region II is the concentration zone of the generated liquid droplets and has a larger surface due to both the generation of local liquids droplets and the impingement with the liquid droplets coming from Region I. Region III is the peripheral ablation zone, which has a smaller surface coverage of the liquid droplets and exhibits liquid droplets in a smaller quantity and also smaller in size. The reason for the morphology in Region III is probably attributed to the much lower temperature in this region since it is mainly from the radiation (see the temperature distribution Region IV in Fig. 4), and the speed of the gas flow is also lower in this region. The comparison between Fig. 4(b) and (d) suggests that the integral of surface coverage of liquid as well as its change is correlated to the temperature distribution.

The statistical distribution of the number of discrete droplets on the plate surface at different ablation times is shown in Fig. 5. At the beginning of the experiment, the surface evolution of the plate material is more influenced by the temperature rather than the gas velocity, the number of discrete droplets increases with a peak appearing at point A. Following by this, in the transition ablation stage, due to the high velocity of the gas flow as well as the generation of more liquid beads, some discrete droplets begin to merge into bigger ones, resulting a drop in the number indicated by point B. In the third stage which is defined as the stabilized stage where the gas flow and the temperature are playing a balanced role, the number of discrete droplets remains almost constant. It also exhibits a transformation of time and space.

3.3. Velocity field of the liquid droplets on the surface

The velocity field of the surface liquid droplets at different ablation times has been previously studied in Ref. [28]. The calculation was carried out using particle image velocity (PIV) method. By using PIV method, it can obviously show the local characteristics, however, it

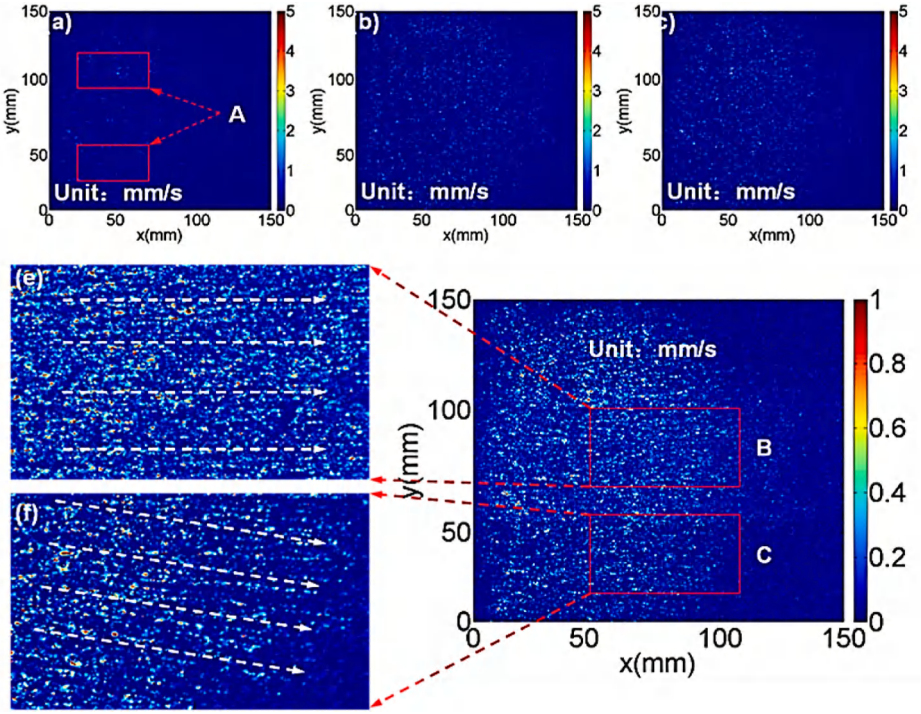

Fig. 6. Liquid velocity field calculated using H–S optical flow method: (a) *R* channel; (b) *G* channel; (c) *B* channel; (d) zoom-in image of sub-image (a); (e–f) zoom-in images corresponding to regions B and C in sub-image (d).

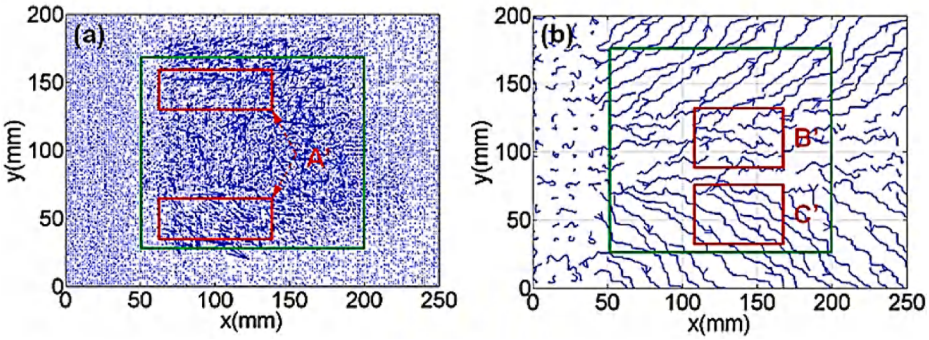

Fig. 7. Vector field calculated using H–S optical flow method: (a) Velocity vector field on surface; (b) surface streamline chart.

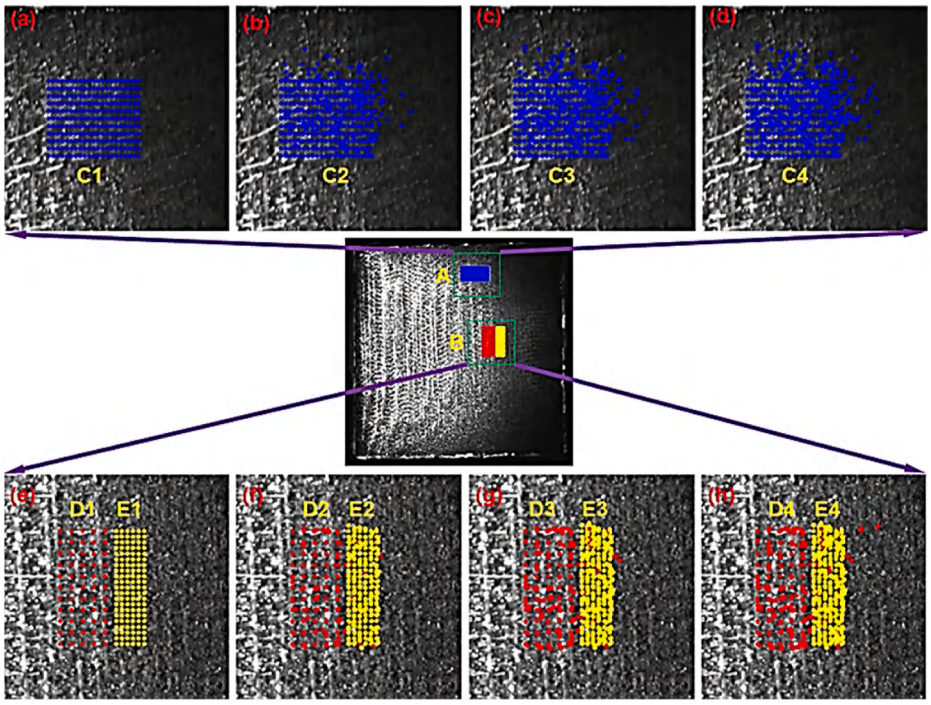

Fig. 8. Characteristic of liquid droplets movement on the plate surface using Lagrangian particle tracking method.

should be noted that the shape characteristics and global velocity of the droplets are not well described due to the fact that the PIV method is based on the particle matching method, which is intrinsically a local feature detection method.

Because the light intensity (including reflection and radiation of liquid drops on the flat plate surface) is much greater than that of the solid itself, therefore, the velocity field of droplets can also be calculated using the optical flow method [29]. Here we adopt the H–S method and show in Fig.8 the velocity field of the liquids on the plate surface. The velocity calculated using *R*, *G*, *B* channels is given in Fig. 6(a-c), respectively. In Fig. 6(d) it shows a zoomed-in area from Fig. 6(a). The rectangular regions in Fig. 6(d) indicated by B and C are further zoomed-in and shown in Fig. 6(e) and (f), respectively. The H–S method well captures the velocity of liquid flow on the plate surface. In addition, the comparison between *R*, *G*, and *B* channels suggests that the result for the velocity field calculated using *R* channel is the best. This is because the radiation intensity of the droplet is greater than that of the solid, and the flat ablative droplet can be analyzed with radiation light, while among the *R*, *G* and *B* channels, the *R* channel is least affected by light source and other factors. As can be seen from Fig. 6(a) and (d), the droplet velocity of region A is relatively larger. The liquid flow direction and its velocity shown in Fig. 6(e-f) agree with the free-jet flow pattern as well as the experimental results.

In Fig. 7, it shows the velocity and streamline chart on the surface. It is noticed that the velocity direction in Fig. 7(a) and the flow direction in Fig. 7(b) are consistent. The regions indicated by A-C in Fig. 6 and those A′-C′ in Fig. 7 show that the droplet velocity map in Fig. 7 has a better size and direction characteristics.

3.4. Characteristics of liquid droplets movement on surface

In Fig. 8 it shows the movement of the surface liquid droplets calculated using Lagrangian particle tracking (LPT) method [30], which displays nicely the flowing characteristics of the droplets over a wide spatial range, namely, it well captures the motion of the droplets from microscale to the macroscopic level. The distribution of the particles (droplets) in Fig. 8(a-h) suggests that the particles in different regions conform to the Newton's second law of movement. In Fig. 8(a-d), the particles exhibit obvious scattering features, which is in accordance with the free-jet theory discussed above. The calculation in Fig. 8(e–h) focuses on the particles flowing in two adjacent regions, as indicated by the dots marked in yellow (D1-4) and red (E1-4). The particles in these

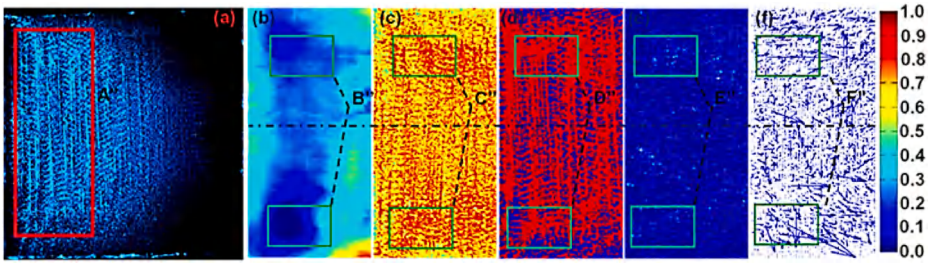

Fig. 9. The flow structure in the core ablation zone on the plate surface: (a) calculated area indicated by the red rectangular; (b) surface height; (c) surface temperature; (d) surface coverage of liquid; (e) surface flow velocity contour; (f) surface velocity vectors. (For interpretation of the references to color in this figure legend, the reader is referred to the Web version of this article.)

two regions exhibit continuous evolution and after certain time, the particles from the red region enter and mix with those in the yellow region, as shown in Fig. 8(h). This agrees with the flowing process of the surface liquid droplets during thermal ablation process. That is, due to the flushing effect of the gas flow, the liquid droplets generated in the upper stream move relatively faster and gradually catch up with the droplets generated downstream and impinge with each other. Similar phenomenon of liquid droplets flow and impingement was also observed during the thermal ablation of C/SiC material [1]. When the red particles pass through the yellow particles, it indicates that there is fusion and fracture in the flow process of droplets. Moreover, the front droplet will transfer to small droplets with the influence of thermal radiation, which are constantly merged by the rear large droplets. In this process, the droplets are grown with the airflow shear force. The higher the droplet height, the greater the airflow shear force. Under the action of airflow shear force and material interface viscosity force, the droplets will split. To calculate the velocity of the droplets during splitting and merging, the continuous droplet was defined as a whole droplet, while the velocities of the two droplets after splitting, were calculated separately.

3.5. Thermal ablation rate

One important criterion for estimating the thermal ablation resistance of the material is the ablation rate. In Fig. 9 it shows the flow field that is normalized with respect to the maximum difference between the smallest and largest values in the core ablation zone on the plate surface. Notice that the region shown in Fig. 9(b-f) corresponds to the area (indicated by red) in Fig. 9(a). The 3D surface height of the specimen at different ablation times shown in Fig. 9(b) was calculated using 3D morphology detection technique and the reconstruction algorithm that is based on Scale Invariant Feature Transform (SIFT), Biharmonic Spline Interpolation (BSI), and 3D DIC technique. First, the initial displacement field is obtained by using SIFT feature point matching, then the full-field deformation information is obtained by using the method of BSI. The temperature filed of the corresponding area in Fig. 9(b) was shown in Fig. 9(c), so is the surface liquid distribution in Fig. 9(d), the surface flow velocity contour in Fig. 9(e), and the velocity vector field of surface liquid in Fig. 9(f).

The surface height in Fig. 9(b) increases non-uniformly due to thermal ablation. This corresponds to a non-uniform thermal ablation rate on the sample surface, with a faster ablation rate in the top and bottom regions. By comparing Fig. 9(b-f), it suggests that the regions that were severely ablated (Fig. 9(b)-B″) are exactly the regions with higher temperature (Fig. 9(c)-C″), higher surface coverage of the liquids (Fig. 9(d)-D″), and higher velocity (Fig. 9(e)-E″).

3.6. Fluid feature of the surface liquid droplets at microscale

Due to the very small size of the liquid droplets on the sample surface, it remains so far a big challenge to capture all the details of the flow behavior of the liquid droplets, especially in high-speed gas flow in wind tunnel. In order to better understand the liquid flow at small scale, we adopt here computational simulation combined with a verification experiment to study the flow behavior of the liquid droplets on the sample surface. The experimental setup is shown in Fig. 10(a), including two cameras, a device for generating wind to flush the liquid droplets, a thin plate surface on which the liquid flows, and a heating furnace for generating liquid droplets. In this work, liquid droplets with high viscosity were simulated with resin materials and the verification experiment was shown in Fig. 10(b). When the resin material on the solid surface was heated to 200 °C in the high temperature furnace, it melted and changed into flow droplets, the air flow (10 m/s-20 m/s) induced by the power device further drove the droplets to move. In order to observe the process of droplet impingement, different droplets were colored. In Fig. 10(b) it captures the process of two droplets that rolling and impinging with each other under the action of the airflow. The result in Fig. 10(c) simulates the liquid flow on the plate surface using experimental conditions given in Fig. 10(a-b). The simulation agrees quite well with the verification experiment and is also consistent with the flat plate ablation test carried out in wind tunnel.

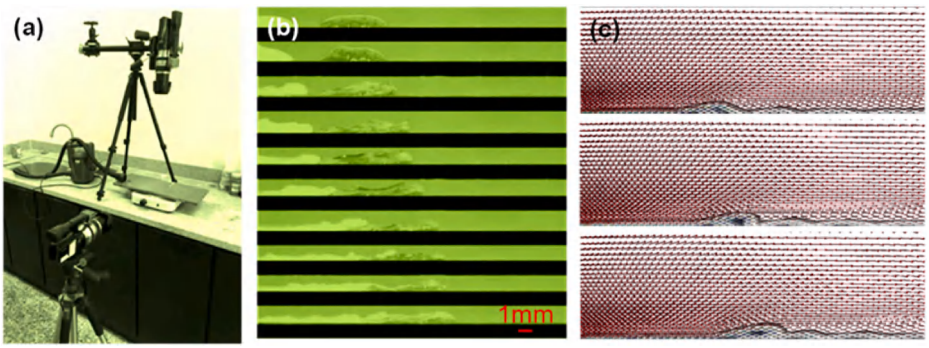

Fig. 10. Flow characterization of liquid droplets: (a) experimental setup; (b) cross-section view of the two droplets with different colors in experiment; (c) cross-section view of the droplets in simulation. (For interpretation of the references to color in this figure legend, the reader is referred to the Web version of this article.)

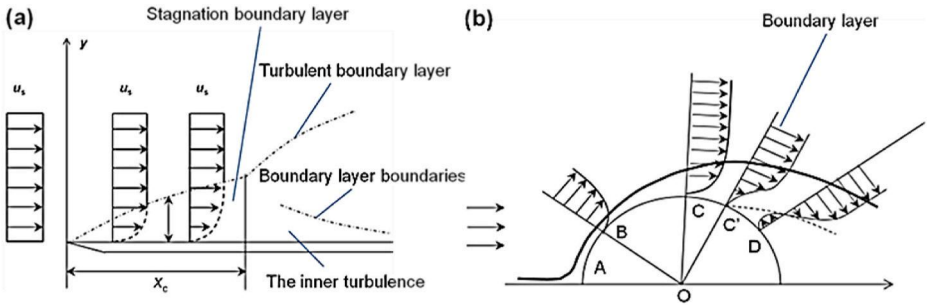

Fig. 11. Flow models: (a) flow on a plate surface; (b) flow on a (half-)circular cylinder.

In order to understand the droplet behavior shown in Fig. 10, we present here in Fig. 11(a-b) two classic fluid-solid interaction models, namely, flow on plate surface in Fig. 11(a) and flow around a (half-) circular cylinder in Fig. 11(b). The comparison between Fig. 11(a) and (b) shows that a friction force will be induced between the plate surface and the liquids with higher viscosity (as in the case for present experiment). Under the friction of the gas flow on plate surface (Fig. 11(a)) the liquids move forward. However, due to the existence of viscous flow of the boundary layer, the liquid droplets have different velocities normal to the plate surface. The cross-section view of the velocity distribution is shown in Fig. 11(b). The velocity gradient results in a driving force for the liquid droplets to move forward in a rolling manner. Both the simulation and verification experiment in Fig. 10(b-c) show that the liquids droplets that were later generated would catch up with, and even climb upon, the earlier generated liquid droplets and then impinge with each other. This process can be viewed as a process of entrainment, rather than a spontaneous impingement due to surface tension.

4. Conclusion

The surface evolution of a flat plate subjected to high temperature thermal ablation in wind tunnel was experimentally observed and analyzed. The liquid generation and flow process on the surface were real time captured using optical technique. The flow characteristics of the generated liquid droplets on the plate surface were analyzed using image processing methods.

(1) The temperature filed on the plate surface was measured using the improved two-color method. It is found that the spatial distribution of the flat surface temperature is correlated to the temporal change.
(2) The image processing method of Level Set was used to extract the liquid droplets that were generated on the surface due to chemical/physical reactions at high temperature. The surface coverage ratio of the droplets and its variation trend along the gas flow direction were correlated with the temperature distribution. Different regions including core area, transition area, and radiation area were defined based on the surface liquid characteristics.
(3) The flow velocity of the liquid droplets on the plate surface was calculated by using H–S optical flow method. Lagrangian particle algorithm was used to simulate the flow process of droplets. It was found that the droplets in the upstream of the gas flow would chase down the droplets generated in the downstream of the gas flow and merge into larger droplets.
(4) The flow of a single droplet and the merging process of two drops were investigated by a verification experiment. The process was then simulated using computational fluid dynamics. The theory of plate surface flow and cylinder surface flow was adopted to analyze the liquid flow and the merging process. It was found that the droplet with high viscosity would generate a great friction force at the interface and result in a velocity gradient normal to the plate surface. The gradient of the velocity could cause the droplet to move forward in a rolling manner. The chasing and merging process of the high viscous liquid droplets is an entrainment process due to the external gas flow instead of a spontaneous merging process due to surface tension.

CRediT authorship contribution statement

Shilong Zhu: Conceptualization, Methodology, Software, Validation, Writing – original draft, Writing – review & editing. **Jinsong Zhang:** Software, Validation, Writing – review & editing. **Mengkun Yue:** Software, Validation, Writing – review & editing. **Yunlong Tang:** Conceptualization, Methodology, Software, Validation, Writing – original draft, Writing – review & editing. **Wen Yue:** Writing – review & editing, Supervision. **Zhe Qu:** Software, Validation, Writing – review & editing. **Xian Wang:** Software, Resources, Data curation. **Lianzhong Chen:** Writing – review & editing, Supervision. **Yewei Gui:** Writing – review & editing, Supervision. **Xue Feng:** Writing – review & editing, Supervision, Project administration, Funding acquisition.

Declaration of competing interest

The authors declare that they have no known competing financial interests or personal relationships that could have appeared to influence the work reported in this paper.

Acknowledgement

We gratefully acknowledge financial support from the National Natural Science Foundation of China (Grant Nos. U20A6001, 11625207, 11921002, and 12102401), and the Fundamental Research Funds for the Central Universities (Grant No. 2652019071).

References

[1] X. Fang, F. Liu, B. Xia, D. Ou, X. Feng, Formation mechanisms of characteristic structures on the surface of C/SiC composites subjected to thermal ablation, J. Eur. Ceram. Soc. 36 (2016) 451–456.
[2] X. Fang, Z. Qu, C. Zhang, X. Feng, In-situ testing of surface evolution of SiC during thermal ablation: mechanisms of formation, flowing and growth of liquid silica beads, Ceram. Int. 43 (2017) 7040–7047.
[3] D. Gunther, S. Jackson, H. Longerich, Laser ablation and arc/spark solid sample introduction into inductively coupled plasma mass spectrometers, Spectrochim. Acta B Atom Spectrosc. 54 (1999) 381–409.
[4] N. Venkatramani, Industrial plasma torches and applications, Curr. Sci. 83 (2002) 254–262.
[5] X. Fang, F. Liu, H. Su, B. Liu, X. Feng, Ablation of C/SiC, C/SiC-ZrO2 and C/SiC-ZrB2 composites in dry air and air mixed with water vapor, Ceram. Int. 40 (2014) 2985–2991.
[6] Y. Wang, X. Xiong, G. Li, H. Liu, Z. Chen, W. Sun, X. Zhao, Ablation behavior of HfC protective coatings for carbon/carbon composites in an oxyacetylene combustion flame, Corrosion Sci. 65 (2012) 549–555.
[7] J. Xie, K. Li, H. Li, Q. Fu, L. Guo, Ablation behavior and mechanism of C/C-ZrC-SiC composites under an oxyacetylene torch at 3000 degrees C, Ceram. Int. 39 (2013) 4171–4178.
[8] S. Ghosh, E. Rhee, J. Avari, P. Woodard, Y. Rudy, Cardiac memory in patients with Wolff-Parkinson-White syndrome - noninvasive imaging of activation and repolarization before and after catheter ablation, Circulation 118 (2008) 907–915.

[9] B. Horn, B. Schunck, Determining optical-flow, Artif. Intell. 17 (1981) 185–203.
[10] B. Lucas, T. Kanade, An iterative image registration technique with an application to stereo vision, Int. Joint Conf. Artif. Intell. 2 (1981) 674–679.
[11] J. Barron, D. Fleet, S. Beauchemin, Performance of optical-flow techniques, Int. J. Comput. Vis. 12 (1994) 43–77.
[12] S. Baker, D. Scharstein, J. Lewis, S. Roth, M. Black, R. Szeliski, A database and evaluation methodology for optical flow, Int. J. Comput. Vis. 92 (2011) 1–31.
[13] D. Thomson, Criteria for the selection of stochastic-models of particle trajectories in turbulent flows, J. Fluid Mech. 180 (1987) 529–556.
[14] K. Korotenko, R. Mamedov, A. Kontar, L. Korotenko, Particle tracking method in the approach for prediction of oil slick transport in the sea: modelling oil pollution resulting from river input, J. Mar. Syst. 48 (2004) 159–170.
[15] J. Wang, Y. Shen, Y. Guo, Seasonal circulation and influence factors of the Bohai Sea: a numerical study based on Lagrangian particle tracking method, Ocean Dynam. 60 (2010) 1581–1596.
[16] H. Su, X. Fang, Z. Qu, C. Zhang, B. Yan, X. Feng, Synchronous full-field measurement of temperature and deformation of C/SiC composite subjected to flame heating at high temperature, Exp. Mech. 56 (2016) 659–671.
[17] M. Natali, M. Monti, J. Kenny, et al., Synthesis and thermal characterization of phenolic resin/silica nanocomposites prepared with high shear rate-mixing technique[J], J. Appl. Polym. Sci. 120 (5) (2015) 2632–2640.
[18] M. Lin, C. Ma, N. Tai, et al., Carbon fiber reinforced phenolic Resin/Silica ceramer composites-processing, mechanical and thermal properties[J], Polym. Compos. 21 (2) (2000) 305–311.
[19] Y. Kong, J. Zhang, M. Yue, et al., Investigation of the bulging mechanism of C/SiC coating through in situ optical observation and numerical simulation[J], Ceram. Int. 47 (14) (2021) 20456–20466.
[20] Y. Tang, M. Yue, J. Zhang, et al., Revealing thermal ablation mechanisms of C/SiC with in situ optical observation and numerical simulation[J], J. Eur. Ceram. Soc. 40 (12) (2020) 3897–3905.
[21] Z. Qu, X. Fang, H. Su, X. Feng, Measurements for displacement and deformation at high temperature by using edge detection of digital image, Appl. Opt. 54 (2015) 8731–8737.
[22] Y. Tang, M. Yue, J. Zhang, et al., Removal of optical crosstalk caused by light source for synchronous measurement of temperature and deformation[J], Opt. Eng. 59 (5) (2020), 054102.
[23] Y. Tang, J. Zhang, M. Yue, et al., Deep learning-based super-resolution images for synchronous measurement of temperature and deformation at elevated temperature[J], Optik - Int. J. Light Electron Opt. 226 (2021) 165764.
[24] Y. Tang, J. Zhang, M. Yue, et al., Temperature and deformation measurement for large-scale flat specimens based on image mosaic algorithms[J], Appl. Opt. (2020) 3145–3154.
[25] A. Abrosimov, Influence of the jet velocity profile on flow characteristics near an obstacle, J. Appl. Mech. Tech. Phys. 29 (1988) 842–848.
[26] H. Zhao, S. Osher, R. Fedkiw, Fast surface reconstruction using the level set method, in: IEEE Workshop on Variational & Level Set Methods, 2001.
[28] Z. Qu, X. Wang, Y. Tang, H. Su, L. Chen, H. Gao, X. Feng, In situ visualization measurement of flat plate ablation in high-temperature gas flow, J. Appl. Mech. 85 (2018).
[29] D. Kesrarat, V. Patanavijit, An Alternative Robust Optical Flow on Dynamic Smoothness Weight (Alpha) of Horn-Schunk Algorithm Using Median Filter with Sub-pixel Displacement, 2013.
[30] F. Bontempi, L. Faravelli, Lagrangian/Eulerian description of dynamic system, Journal Of Engineering Mechanics-Asce 124 (1998) 901–911.